Catalysis Science & Technology

ROYAL SOCIETY OF CHEMISTRY

PAPER

View Article Online
View Journal | View Issue

Cite this: *Catal. Sci. Technol.*, 2022, 12, 3594

Structure–activity correlation in aerobic cyclohexene oxidation and peroxide decomposition over $Co_xFe_{3-x}O_4$ spinel oxides†

Julia Büker,[a] Steven Angel,[b] Soma Salamon, [c] Joachim Landers, [c] Tobias Falk,[a] Heiko Wende, [c] Hartmut Wiggers,*[b] Christof Schulz,[b] Martin Muhler [ad] and Baoxiang Peng *[ad]

Received 16th March 2022,
Accepted 21st April 2022

DOI: 10.1039/d2cy00505k

rsc.li/catalysis

Nanoparticulate $Co_xFe_{3-x}O_4$ ($0 \leq x \leq 3$) catalysts were prepared by spray-flame synthesis and applied in liquid-phase cyclohexene oxidation with O_2 as oxidant. The catalysts were characterized in detail using N_2 physisorption, XRD, TEM, XPS, FTIR, Raman, and Mössbauer spectroscopy. A volcano plot was obtained for the catalytic activity in cyclohexene oxidation as a function of the Co content with a maximum at $x = 1$. Thus, $CoFe_2O_4$ achieved the highest degree of cyclohexene conversion and the fastest decomposition rate of the key intermediate 2-cyclohexene-1-hydroperoxide. Kinetic studies and a stability test were performed over $CoFe_2O_4$, showing that cyclohexene oxidation follows first-order kinetics with an apparent activation energy of 58 kJ mol^{-1}. The catalytic hydroperoxide decomposition during cyclohexene oxidation was further investigated using H_2O_2 and *tert*-butyl hydroperoxide as simpler surrogates resulting in similar volcano-type correlations. The increase in catalytic activity with increasing Fe content with a maximum at $x = 1$ is ascribed to the increasing concentration of octahedrally coordinated Co^{2+} cations in the spinel structure leading to the presence of coordinatively unsaturated Co_{3c}^{2+} surface sites, which are identified to be the most active sites for 2-cyclohexene-1-hydroperoxide decomposition in cyclohexene oxidation.

Introduction

The oxidation of olefins is a key technology in the chemical industry, as the formed products are important building blocks for the synthesis of fine and bulk chemicals, comprising agrochemicals, pharmaceuticals, fragrances, and polymers.[1,2] In particular, the oxidation of cyclohexene provides access to valuable oxygenated products, such as 2-cyclohexene-1-one, 2-cyclohexene-1-ol, cyclohexane-1,2-diol, and cyclohexene oxide.[2,3] Industrial processes are mainly conducted in the gas phase under harsh reaction conditions and operated at low conversion to retain high selectivity and to suppress total oxidation. In contrast, liquid-phase reactions can be carried out under milder reaction conditions leading to higher selectivities. Nevertheless, aerobic cyclohexene oxidation is subject to a complex reaction network because of the two active centres in the cyclohexene molecule (Scheme 1). When allylic oxidation takes place at the C–H bond, cyclohexene is oxidized to 2-cyclohexene-1-hydroperoxide, which can further react to 2-cyclohexene-1-ol, 2-cyclohexene-1-one and 7-oxabicyclo[4.1.0]-heptane-2-one. On the other hand, epoxidation can occur at the olefinic C=C bond, yielding cyclohexene oxide and cyclohexane-1,2-diol. Moreover, both reaction pathways cannot be clearly separated, because 2-cyclohexene-1-hydroperoxide formed within the allylic pathway can react with another cyclohexene molecule resulting in the formation of cyclohexene oxide, which is typically referred to the epoxidation pathway. Early studies

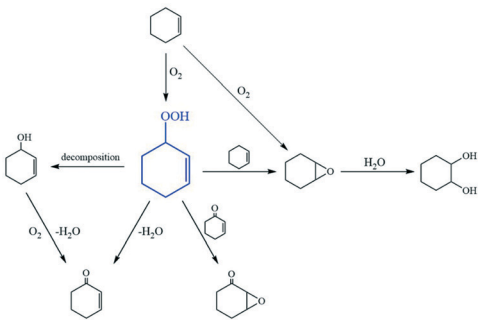

Scheme 1 Reaction network of cyclohexene oxidation.

[a] *Laboratory of Industrial Chemistry, Ruhr University Bochum, 44780 Bochum, Germany. E-mail: baoxiang.peng@techem.rub.de*
[b] *IVG Institute for Combustion and Gas Dynamics – Reactive Fluids and CENIDE Center for Nanointegration, University of Duisburg-Essen, 47057 Duisburg, Germany. E-mail: hartmut.wiggers@uni-due.de*
[c] *Faculty of Physics, University of Duisburg-Essen, 47057 Duisburg, Germany*
[d] *Max Planck Institute for Chemical Energy Conversion, 45470 Mülheim an der Ruhr, Germany*

† Electronic supplementary information (ESI) available. See DOI: https://doi.org/10.1039/d2cy00505k

identified 2-cyclohexene-1-hydroperoxide to be an unstable reaction intermediate of cyclohexene oxidation. Already in 1939, Criegee *et al.* detected 2-cyclohexene-1-hydroperoxide to be the main product of cyclohexene autoxidation and clarified its structure.[4] Sridhar and coworkers investigated the uncatalyzed decomposition of 2-cyclohexene-1-hydroperoxide and found 2-cyclohexene-1-ol and 2-cyclohexene-1-one to be the main products even in the absence of O_2.[5] It can therefore be deduced that the aerobic oxidation of cyclohexene at least partially occurs autocatalytically forming 2-cyclohexene-1-hydroperoxide with high selectivity.

The autoxidation of cyclohexene renders the decomposition of the hydroperoxide intermediate to be the key step for selective cyclohexene oxidation. Thus, the use of a heterogeneous catalyst offers the possibility to selectively decompose 2-cyclohexene-1-hydroperoxide into one of the desired products, enabling the formation of high-value chemicals in high yields.

For this purpose, highly active catalysts are needed. Transition metal oxides have raised much interest because of their low cost and their potential to replace conventional noble metal catalysts. Especially, oxides with spinel structure were found to be highly stable under extreme reaction conditions and flexible with regard to the variety of metal ions with different valencies incorporated into their lattices.[6] Spinel oxides consist of a close-packed cubic lattice of oxygen anions with the general formula AB_2O_4, where A can be a group IIA metal or a transition metal cation with the oxidation state 2+ and B is a group IIIA metal or transition metal cation in the 3+ oxidation state. In a normal spinel structure like ideal Co_3O_4, the A^{2+} ions occupy one-eighth of the tetrahedral holes and the 3+ species occupy half of the octahedral voids. In contrast, within an inverse spinel such as ideal $CoFe_2O_4$, the A^{2+} ions and half of the B^{3+} ions exchanged their positions.[7]

In addition to the occupation of octahedral and tetrahedral sites within the spinel structure, the particle size and the resulting facets of the particles also play an important role. While it is generally accepted that conversion increases with increasing specific surface area, our recent studies show that larger Co_3O_4 particles with consequently smaller surface areas can nevertheless lead to higher conversion due to the exposure of catalytically more active facets with, for example, multiple coordinatively unsaturated Co_{cus}^{3+} sites.[8]

Because of their high stability, their large variety of materials and also semiconducting properties, spinel oxides are applied in many fields, such as Li-ion batteries,[9] photodegradation of pollutants,[10] water oxidation,[11] and electrochemical oxygen evolution reaction.[12] In addition, Co-based transition metal oxides have already been applied in liquid-phase oxidation reactions in our previous studies.[13–17]

Spinel oxides can be synthesized by several methods, such as mixed powder synthesis,[7] co-precipitation,[18] sol–gel synthesis,[19] hydrothermal synthesis,[20] and spray and freeze drying.[21] Among these methods, the continuous and scalable spray-flame synthesis is a suitable method providing high specific surface areas, small nanoparticle sizes, and well-controlled catalyst compositions.[13,22]

In the present work, we report on the liquid-phase oxidation of cyclohexene in acetonitrile with molecular O_2 over a series of spray-flame synthesized $Co_xFe_{3-x}O_4$ spinel nanoparticles under mild conditions. To date, to the best of our knowledge, no comparable study has been reported on the liquid-phase cyclohexene oxidation over mixed Co–Fe spinel oxides. We aim at understanding the effect of Fe substitution into the Co_3O_4 spinel structure on the reaction mechanism of cyclohexene oxidation. The $Co_xFe_{3-x}O_4$ nanoparticulate materials were characterized in detail, and their catalytic properties were systematically elaborated. Kinetic investigations, a reusability test and the influence of H_2O were studied over the best-performing catalyst $CoFe_2O_4$. The decomposition of H_2O_2 and *tert*-butyl hydroperoxide (TBHP) was carried out to mimic the decomposition of the key intermediate 2-cyclohexene-1-hydroperoxide to correlate the rates of cyclohexene oxidation and peroxide decomposition and, thereby, identify the active sites.

Results and discussion

Catalyst characterization

A series of $Co_xFe_{3-x}O_4$ (x = 0, 0.5, 1, 1.5, 2, 2.5, 3) nanoparticulate materials was synthesized by spray-flame synthesis using dissolved metal nitrates as precursors with a concentration of 0.2 M. The detailed synthesis procedure can be found elsewhere.[13,23] After synthesis, the samples were heat-treated at 250 °C for 2 h in air to remove adsorbed organic and water residuals from the particles surface.

The N_2 physisorption-derived specific surface areas determined by applying the BET equation were high, ranging between 87 and 151 $m^2\ g^{-1}$ (Table 1). Assuming monodisperse and spherical particles, average particle sizes of 8.3 to 12.0 nm were calculated (Table 1). The count mean diameters based on TEM images resulted in particle sizes between 8.4 and 11.1 nm with homogeneous particle size distributions, which are in agreement with the BET-based particle sizes (Table 1). Nevertheless, according to the analyzed TEM images, besides spherical particles, a reasonable number of faceted particles were identified (Fig. S1†). All catalysts show a single crystalline nanostructure with high crystallinity but crystallographically disordered structures (Fig. 1 and S1†). The EDX elemental mapping identified a homogeneous distribution of Co and Fe for all samples (Fig. S3†) and on average, the experimental Co/Fe ratios were similar to the desired nominal ones summarized in Table 1.

The HAADF-TEM images of Co_3O_4 and $CoFe_2O_4$ were used to determine the lattice spacings of the spinel nanoparticles. For Co_3O_4, a distance of d = 0.234 nm was recorded in agreement with the theoretical lattice spacing of d_{100} = 0.24 nm (Fig. S2†).[24] For $CoFe_2O_4$, a significantly higher number of hexagonal shaped particles was found, indicating (111)

Table 1 Specific surface areas, particle sizes determined by N_2 physisorption and TEM, bulk and surface Co/(Co + Fe) ratios based on EDX and XPS analyses of the $Co_xFe_{3-x}O_4$ samples

Sample	Specific surface area [$m^2\ g^{-1}$]	Particle size[a] [nm]	Particle size[b] [nm]	Co/(Co + Fe)[c]	$x(Co_xFe_{3-x}O_4)$[c]	Co/(Co + Fe)[d]	$x(Co_xFe_{3-x}O_4)$[d]
Co_3O_4	118	8.3	11.1	1	3	1	3
$Co_{2.5}Fe_{0.5}O_4$	87	12.0	8.8	0.82	2.47	0.84	2.51
$Co_2Fe_1O_4$	128	8.3	8.8	0.67	2.01	0.68	2.04
$Co_{1.5}Fe_{1.5}O_4$	151	7.5	8.4	0.51	1.54	0.52	1.55
$Co_1Fe_2O_4$	129	8.8	8.7	0.33	0.99	0.36	1.07
$Co_{0.5}Fe_{2.5}O_4$	122	9.4	9.9	0.18	0.53	0.18	0.55
γ-Fe_2O_3	111	10.5	9.2	0	0	0	0

[a] Estimated from the specific surface areas assuming spherical particles. [b] Determined by TEM. [c] Determined by EDX. [d] Determined by XPS.

surfaces.[25] The determined lattice spacings of 0.509, 0.476 and 0.480 nm agree with the theoretical value of d_{111} = 0.484 nm, suggesting that (111) surfaces are dominant for $CoFe_2O_4$.[26] Whereas (100)-oriented surfaces expose coordinatively unsaturated metal cations, which are fivefold coordinated at the octahedral sites of the spinel (M^O_{5c}), those octahedrally coordinated metal cations are only threefold coordinated at the (111) surfaces (M^O_{5c}).[25] Metal cations with a lower coordination number are assumed to be more catalytically active.

XRD patterns were recorded for the $Co_xFe_{3-x}O_4$ catalysts (Fig. 2). A cubic spinel structure was identified for all samples. For Co_3O_4, the pattern fits better to the reference pattern of a cobalt-deficient spinel phase than to stoichiometric Co_3O_4. With increasing Fe content, the reflections start shifting to lower 2θ angles as expected. Based on the XRD patterns, the iron oxide sample (x = 0) cannot be clearly identified, because the magnetite (Fe_3O_4) and maghemite (γ-Fe_2O_3) phases have both almost identical lattice parameters. Crystal structure analysis was performed by Rietveld refinement resulting in lattice parameters, which amount to 8.08, 8.38 and 8.36 Å, well-fitting to the literature-reported values of 8.08,[27] 8.38,[28] and 8.35 Å (ref. 29) for Co_3O_4, $CoFe_2O_4$ and γ-Fe_2O_3, respectively. The reported lattice constant of Fe_3O_4 is 8.39 Å,[29] indicating the presence of γ-Fe_2O_3 instead of Fe_3O_4 (Fig. S4†).

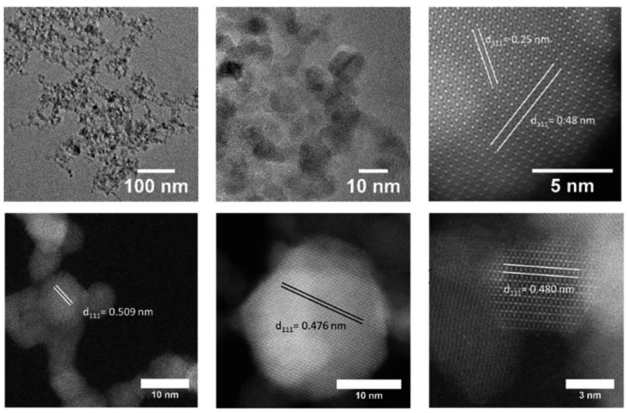

Fig. 1 TEM and HAADF-STEM images of $CoFe_2O_4$ with lattice spacings.

Raman spectroscopy was applied to investigate the electronic structure and the cation occupation of the tetrahedral and octahedral sites in the spinel structure of the $Co_xFe_{3-x}O_4$ samples (Fig. 3). The recorded spectra clearly show five bands, which can be assigned to A_{1g}, E_g and three F_{2g} phonon modes originating from lattice vibrations of the cubic spinel structure. With increasing Fe amount in the samples from Co_3O_4 to $Co_{1.5}Fe_{1.5}O_4$, a redshift of the A_{1g} mode was observed corresponding to the symmetric Co^{3+}–O stretching vibration of the octahedral sites, which indicates a lower occupancy of Co^{3+} ions at octahedral sites and a starting phase transition towards an inverse spinel.[30,31] The intensity of the $F_{2g}(3)$ mode at 195 cm^{-1} also decreased, indicating the lower occupation of tetrahedral voids by Co^{2+} ions.[32] Similarly, the intensity of the E_g mode at 481 cm^{-1}, corresponding to different motions of the AO_4-tetrahedral unit,[31] also decreased. The $F_{2g}(3)$ mode at 475 cm^{-1} of $Co_{0.5}Fe_{2.5}O_4$ and $CoFe_2O_4$ corresponds to the vibration of Co^{2+} ions in octahedral voids,[33] while the $A_{1g}(1)$ mode (688 cm^{-1}) of both samples corresponds to the symmetric

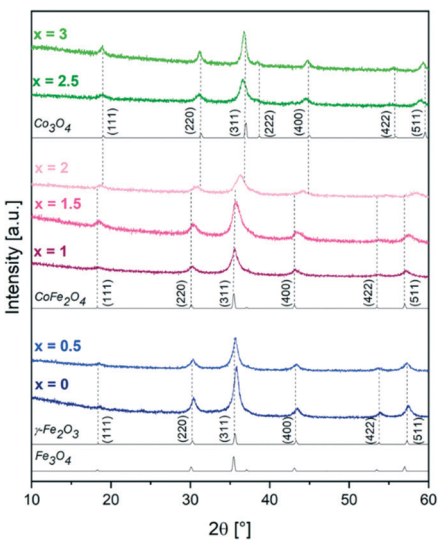

Fig. 2 XRD patterns of the $Co_xFe_{3-x}O_4$ (x = 0, 0.5, 1, 1.5, 2, 2.5, 3) samples and corresponding reference patterns taken from the ICSD database (Co_3O_4: ICSD 36256, $CoFe_2O_4$: ICSD 109044, Fe_3O_4: ICSD 26410, γ-Fe_2O_3: ICSD 172906).

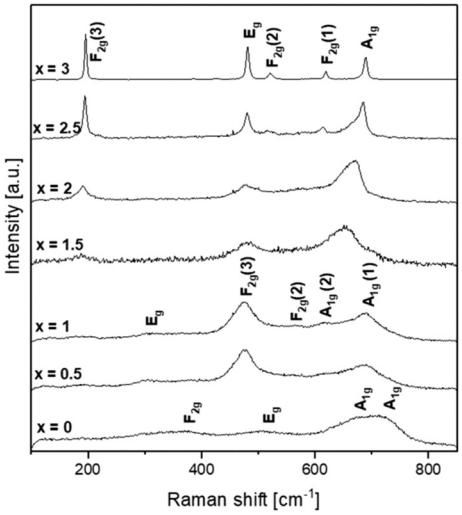

Fig. 3 Raman spectra of the $Co_xFe_{3-x}O_4$ (x = 0, 0.5, 1, 1.5, 2, 2.5, 3) samples.

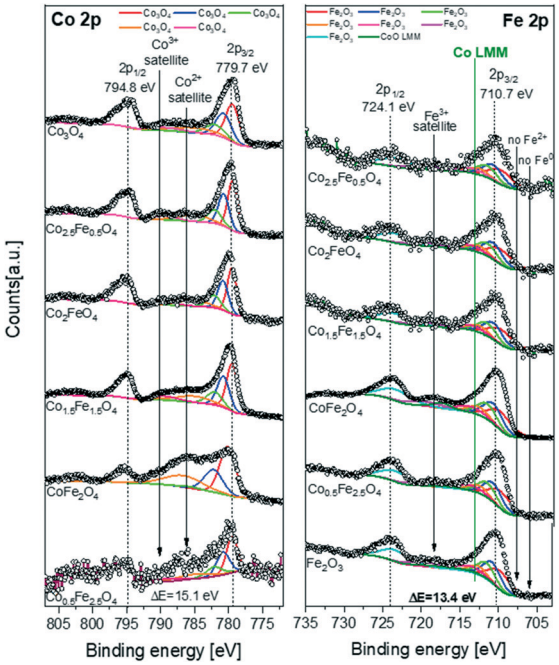

Fig. 4 XP spectra of the Co 2p and Fe 2p of the $Co_xFe_{3-x}O_4$ (x = 0, 0.5, 1, 1.5, 2, 2.5, 3) samples.

stretching of oxygen atoms with respect to Fe^{3+} cations in tetrahedral voids.[34] The Raman spectrum of the iron oxide sample indicates the formation of the Fe_3O_4 and the γ-Fe_2O_3 phase,[28] which is a Fe^{2+}-vacant spinel structure. It is deduced that the samples $CoFe_2O_4$, $Co_{0.5}Fe_{2.5}O_4$ and γ-Fe_2O_3 have a predominantly inverse spinel structure.

FTIR spectra were recorded in the frequency range between 800 and 400 cm^{-1}, reflecting fundamental vibrations of metal–oxygen bonds in crystalline solids (Fig. S5†). The two bands for normal Co_3O_4 at 656 and 552 cm^{-1} fit to previously reported values corresponding to Co^{2+} in tetrahedral and octahedral voids, respectively.[35] The band at 541 cm^{-1} for inverse γ-Fe_2O_3 is assigned to tetrahedrally coordinated Fe^{3+}, while the band at 381 cm^{-1} originates from octahedral Fe^{3+}.[36,37] The shifting and vanishing of the recorded signals shows the transition from normal to inverse spinel with increasing Fe amount incorporated into the Co_3O_4 spinel structure.

The $Co_xFe_{3-x}O_4$ samples were further characterized using X-ray photoelectron spectroscopy (XPS) to examine the oxidation states and the surface composition of the catalysts. The Co 2p region in Fig. 4 shows the Co $2p_{1/2}$ and Co $2p_{3/2}$ signals at 794.8 and 779.7 eV, respectively.[38] The intense shake-up satellite peak at 787 eV can be assigned to Co^{2+}, which was increasing with increasing Fe amount. Co^{3+}only exhibits a weak satellite peak at 790 eV indicating a decrease in Co^{3+} concentration with increasing Fe amount.[14] For the samples $Co_{0.5}Fe_{2.5}O_4$ and $CoFe_2O_4$, only Co^{2+} was identified as expected, whereas the other samples contain mixed Co^{2+}/Co^{3+} oxidation states. For Co_3O_4, a value of 60% Co^{2+} was determined with respect to the total Co amount on the catalysts' surface. Fig. 4 displays the Fe $2p_{1/2}$ and $2p_{3/2}$ peaks at 724.1 and 710.7 eV, respectively. The peak intensities gradually increased with increasing Fe amount in the $Co_xFe_{3-x}O_4$ samples. The positions of the $2p_{3/2}$ peak and the satellite peak at 718.4 eV indicate the presence of Fe^{3+} for all samples. For Fe^{2+}, both peaks would be shifted to lower binding energies.[14,39] The C 1s region shows a distinct peak at 284.5 eV, which corresponds to C–C bonds and was used as a reference for calibration. The O 1s peak at 529.5 eV can be fitted by contributions of bulk and surface O (Fig. S6†). The surface composition of the $Co_xFe_{3-x}O_4$ samples is summarized in Table S1.† The calculated surface Co/Fe ratios based on the XPS measurements agree with the bulk Co/Fe ratio determined by EDX, indicating similar bulk and surface compositions for all samples (Table 1).

Mössbauer spectroscopy measurements at 4.3 K were performed to additionally identify and verify the oxidation state of Fe in the $Co_xFe_{3-x}O_4$ samples (Fig. S7†) with the applied methodology for evaluation of experimental spectra being illustrated in the ESI† in detail. A magnetically ordered sextet structure was recorded, which can be reproduced sufficiently for most of the samples by two subspectra representing the spinel tetrahedral A- and octahedral B-site. The sites were identified by their characteristic isomer shifts of $\delta \approx 0.37$ mm s^{-1} for the A-site and $\delta \approx 0.47$ mm s^{-1} for the B-site relative to α-Fe at room temperature.[40,41] As no third subspectrum, which could be assigned to Fe^{2+} ions, was observed for any sample, only Fe^{3+} was identified in agreement with the XPS results. While for $x \geq 1$ no Fe^{2+} is to be expected due to the presence of Co^{2+}, the absence of Fe^{2+} for $x = 0$ indicates that this sample is oxidized to maghemite (γ-Fe_2O_3). Upon rising the Co-fraction x, a gradual change in the structure of the Mössbauer spectra can be observed, resulting in lower average hyperfine magnetic fields B_{hf} visible in Fig. S7A,† as well as increasing spin canting due to the enhanced magnetic anisotropy of $CoFe_2O_4$ and the trend towards antiferromagnetic ordering of Co_3O_4 for higher

values of x (Fig. S7B†). Fe ion site occupation can be extracted directly from the relative A- and B-site subspectral intensities and thereby, the distribution of Co^{2+} ions on the different lattice positions can be inferred up to $x = 3$ when assuming that Co^{3+} is placed on octahedral positions exclusively, as illustrated in the ESI.† Following this approach, inversion parameters in the range of *ca.* 0.75 were found for $x \lesssim 1$, pointing towards the tendency of Co^{2+} to be placed preferably on octahedral sites, corresponding more closely to the inverse spinel structure. For $x > 1$ the inversion parameter gradually decreases, as Co^{3+} is placed on B-site positions, reaching a minimum value of *ca.* 0.25 for $x = 2.5$ when approaching the normal spinel structure of Co_3O_4.[42] Here, one has to consider that for $x \gtrsim 1.5$, due to the increasing spin frustration, applying the external field no longer yields better subspectral resolution. Still, even from zero field spectra, general trends in site occupancy can be extracted to some degree, displaying an evolution in the inversion parameter consistent with results from Raman spectroscopy.

In summary, we successfully synthesized a series of $Co_xFe_{3-x}O_4$ catalysts with chemical compositions close to the nominal ones, high specific surface areas ranging from 87 to 151 $m^2\ g^{-1}$, and small particle sizes between 8.3 and 12.0 nm. XRD measurements identified phase-pure samples of a cubic spinel structure. For $x = 0$, Rietveld refinement and Raman spectroscopy indicated the presence of the Fe^{2+}-vacant structure γ-Fe_2O_3. XPS and Mössbauer measurements both demonstrated the absence of Fe^{2+} species in all samples. Raman and Mössbauer spectroscopy showed the tendency of Co_3O_4, $Co_{2.5}Fe_{0.5}O_4$ and Co_2FeO_4 towards the normal spinel phase, whereas $CoFe_2O_4$, $Co_{0.5}Fe_{2.5}O_4$ and γ-Fe_2O_3 were found to have a predominantly inverse spinel structure. The lattice spacing of $CoFe_2O_4$ indicates a dominant (111) surface, exposing coordinatively unsaturated M_{5c}^{O} metal sites.

Cyclohexene oxidation over $Co_xFe_{3-x}O_4$

The catalytic properties of the $Co_xFe_{3-x}O_4$ nanoparticulate spinel catalysts in cyclohexene oxidation were studied under mild reaction conditions in acetonitrile using molecular O_2 as oxidizing agent. Initial experiments on the variation of the stirring speed showed that a speed of agitation of 600 rpm is suitable to exclude external mass transfer limitation (Fig. S8†).

After 6 h, all catalysts revealed a moderate to high catalytic activity with degrees of conversion ranging from 44 to 69% (Fig. S9†), which is comparable to the degree of conversion (75%) over spray-flame synthesized $LaCoO_3$ perovskite oxides.[13,16] The comparison of Co_3O_4 and γ-Fe_2O_3 clearly shows the superior activity of the Co-containing catalyst after 6 h. In cyclohexene oxidation, Co_3O_4 achieved a significantly enhanced conversion as well as a lower selectivity to 2-cyclohexene-1-hydroperoxide. These results indicate a faster hydroperoxide decomposition, leading to an increase in 2-cyclohexene-1-one selectivity. In contrast, cyclohexene oxidation over γ-Fe_2O_3 was characterized by a slow hydroperoxide decomposition, so that the ketone selectivity is lowered by 12% in comparison to Co_3O_4.

The comparison of the $Co_xFe_{3-x}O_4$ catalysts containing both Co and Fe clearly shows a positive effect of Fe substitution on the initial catalytic activity (Fig. 5). With increasing Fe amount up to $CoFe_2O_4$ ($x = 1$), the degree of conversion gradually increased from 14.3 to 23.0% after 0.5 h, whereas a blank reaction resulted in only 4.8% conversion (Fig. S10†). The increase in conversion was accompanied by a decreased hydroperoxide selectivity by 24.5%, indicating a faster decomposition, which results in higher product yields. However, the product selectivity was not affected, leading to the assumption that the catalyst is mainly involved in the formation and decomposition of the intermediate 2-cyclohexene-1-hydroperoxide. When the Fe content is further increased beyond $CoFe_2O_4$ ($x < 1$), the catalytic activity dropped as shown by the low degree of conversion of 14.4%, and the hydroperoxide selectivity became the highest within the whole catalyst series at 75.5%, identifying γ-Fe_2O_3 to be least active for cyclohexene oxidation.

The correlation of specific surface areas and particle sizes of the investigated catalysts with their catalytic activity excludes strong microstructural effects (Fig. S11†).

The comparison with the catalytic activity of spray-flame-synthesized $LaCoO_3$ nanoparticles for cyclohexene oxidation we presented in a previous study indicates a comparable catalytic activity of the herein presented $CoFe_2O_4$ nanoparticles but a lower selectivity to 2-cyclohexene-1-hydroperoxide.[13] Compared to other Co-based catalysts presented in literature reports, our $CoFe_2O_4$ achieves significantly higher degrees of conversion at similar or shorter reaction times (Table S2†).

The $CoFe_2O_4$ catalyst was chosen for further kinetic investigations, as it had the highest catalytic activity in cyclohexene oxidation with molecular O_2. As expected, a strong influence of temperature on cyclohexene oxidation was observed (Fig. S12†). Cyclohexene conversion was limited to

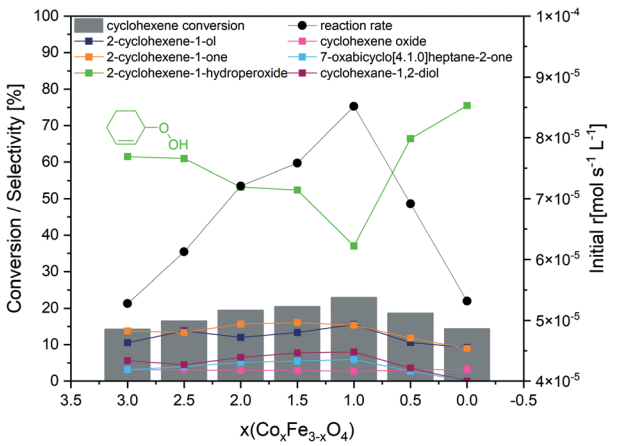

Fig. 5 The influence of Fe substitution into $Co_xFe_{3-x}O_4$ spinel catalysts on cyclohexene conversion, product selectivity and initial reaction rate. Reaction conditions: 20 mmol cyclohexene, 30 mL acetonitrile, 50 mg catalyst, 80 °C, 10 bar O_2, 600 rpm, 0.5 h.

38.7% at 60 °C, whereas at 100 °C nearly full conversion of 91.4% was recorded after 6 h. Additionally, hydroperoxide decomposition strongly increased at higher temperatures, resulting in its complete decomposition at 100 °C. Thus, product selectivity is enhanced and 2-cyclohexene-1-one becomes the main product of cyclohexene oxidation with a selectivity of 28.2%. Meanwhile, 2-cyclohexene-1-ol selectivity decreased, indicating the further oxidation of 2-cyclohexene-1-ol to the corresponding ketone. This led to strongly increasing ketone/alcohol ratios, which amount to 1.9 at 60 °C and 7.6 at 100 °C. However, the product distribution within the epoxidation products was not that strongly affected by temperature, as the cyclohexene-1,2-diol/cyclohexene oxide ratio only slightly decreased from 3.2 to 2.5. Nevertheless, higher temperatures shifted cyclohexene oxidation to the epoxidation pathway, as the ratio of allylic/epoxidation products decreased from 3.2 to 1.3. The catalytic data at different temperatures were used for the Arrhenius analysis. The degrees of cyclohexene conversion at different temperatures as a function of time are shown in Fig. 6A. Based on previous studies, cyclohexene oxidation over transition metal oxide catalysts is assumed to follow first-order reaction kinetics.[13,16] The linearized plots based on first-order reaction kinetics were well suited for linear regression ($R^2 > 0.98$), suggesting that cyclohexene oxidation over $CoFe_2O_4$ follows first-order reaction kinetics (Fig. S12D†).

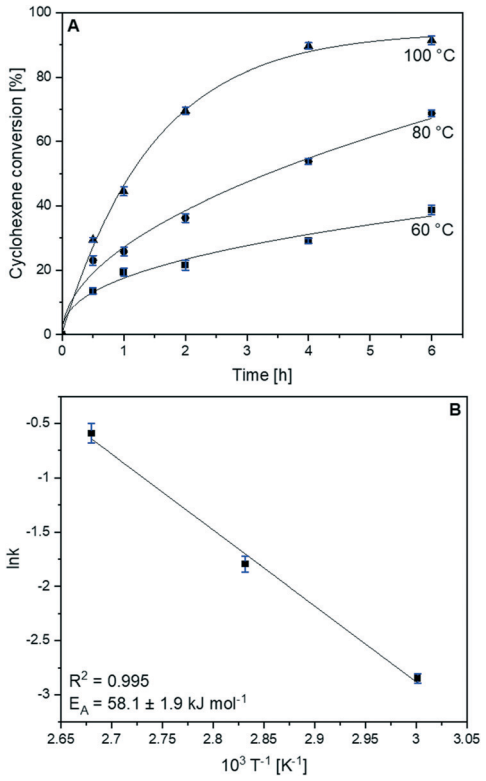

Fig. 6 Kinetic investigations of cyclohexene oxidation over $CoFe_2O_4$. (A) Cyclohexene conversion as a function of time at different temperatures, and (B) the Arrhenius plot based on first-order kinetics. The rate constants *k* were determined according to Fig. S12D.† Reaction conditions: 20 mmol cyclohexene, 30 mL acetonitrile, 50 mg catalyst, 10 bar O_2, 600 rpm, 6 h.

The Arrhenius analysis resulted in an apparent activation energy of 58.1 kJ mol^{-1} (Fig. 6B). A reusability test was carried out to investigate the stability of the $CoFe_2O_4$ catalyst in terms of cyclohexene conversion and product selectivity (Fig. S13†). Four oxidation runs were performed, resulting in high and essentially equal degrees of cyclohexene conversion between 66.9 and 68.0%, which is in the range of experimental error and identifies $CoFe_2O_4$ to be a highly reusable catalyst under these mild oxidation conditions. Only a slight decrease in hydroperoxide decomposition by 5% was observed after the second run, resulting in a lower selectivity to 2-cyclohexene-1-one, indicating that the catalyst plays a crucial role in hydroperoxide decomposition. After the reusability test, a similar XRD pattern of phase-pure spinel structure of high crystallinity (Fig. S14†) and similar TEM images (Fig. S15†) were recorded, confirming the high stability of $CoFe_2O_4$ during cyclohexene oxidation.

As water is produced as a by-product in several reaction steps of cyclohexene oxidation, its influence on the catalytic activity was investigated by adding water to the initial reaction mixture (Fig. S16†). The initial reaction rate of cyclohexene oxidation was clearly suppressed. Nevertheless, cyclohexene conversion was only lowered by 5% after 6 h, and the hydroperoxide selectivity increased at low reaction times but reached a comparable value after 6 h. This was observed for almost all reaction products, indicating that H_2O may block the active sites of $CoFe_2O_4$ at the beginning of the reaction, but the adsorption of the reactant is favored.

Mimicking 2-cyclohexene-1-hydroperoxide decomposition

Cyclohexene oxidation underlies an enormously complex reaction network, in which 2-cyclohexene-1-hydroperoxide plays a key role. The decomposition of 2-cyclohexene-1-hydroperoxide can lead to the formation of several reaction products (Scheme 1). Thus, the heterogeneously catalyzed decomposition of the hydroperoxide intermediate is the main target for selective cyclohexene oxidation. Within cyclohexene oxidation reactions, the hydroperoxide decomposition rate may be influenced by many factors, as the reaction mechanism and several correlations within the reaction network have not been fully clarified yet. Therefore, we implemented less complex peroxide decomposition reactions to mimic the hydroperoxide decomposition kinetics during cyclohexene oxidation over the $Co_xFe_{3-x}O_4$ catalysts using H_2O_2 and TBHP as surrogates (Fig. S17†). Fig. S18† shows the evolved O_2 volume as a function of time for both reactions. To avoid microstructural effects, the initial reaction rates normalized to the surface areas of the catalysts were calculated (Fig. 7). For H_2O_2 and TBHP decomposition, $CoFe_2O_4$ exhibited the highest reaction rates, whereas pure Co_3O_4 and γ-Fe_2O_3 showed a low catalytic activity, which is in agreement with the catalytic results of cyclohexene oxidation. Thus, these results indicate a synergistic effect of Co and Fe

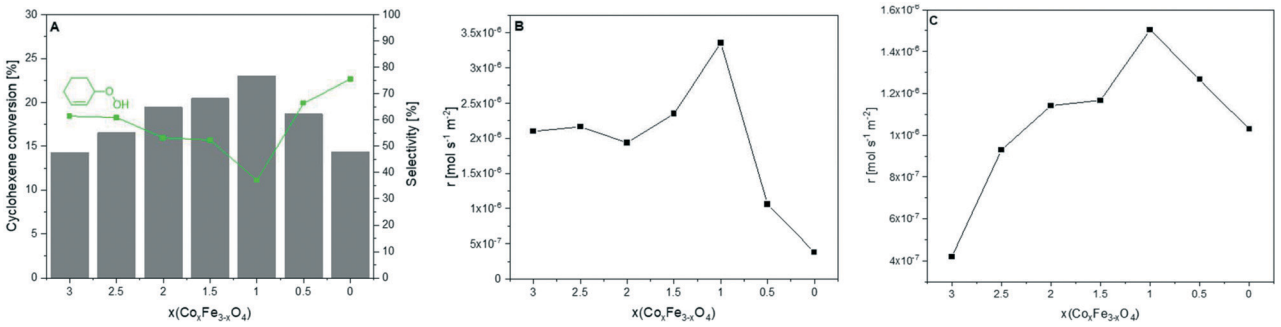

Fig. 7 (A) Volcano plots as a function of Co content for cyclohexene conversion and selectivity to 2-cyclohexene-1-hydroperoxide after 0.5 h, (B) initial reaction rates of H_2O_2 decomposition after 3 min and (C) initial reaction rates of TBHP decomposition after 5 min normalized to the surfaces areas of the $Co_xFe_{3-x}O_4$ catalysts.

in $Co_xFe_{3-x}O_4$ nanoparticles, which improves the decomposition rates of hydroperoxides such as 2-cyclohexene-1-hydroperoxide, TBHP and H_2O_2, resulting in the following activity ranking of the catalysts:

CHHP:	Co_1>	$Co_{1.5}$>	Co_2>	$Co_{2.5}$>	Co_3>	$Co_{0.5}$>	Co_0
H_2O_2:	Co_1>	$Co_{1.5}$>	Co_2>	$Co_{2.5}$>	Co_3>	$Co_{0.5}$>	Co_0
TBHP:	Co_1>	$Co_{1.5}\approx$	$Co_{0.5}$>	Co_2>	Co_0>	$Co_{2.5}$>	Co_3

The $Co_xFe_{3-x}O_4$ catalysts show an equal order of activity for 2-cyclohexene-1-hydroperoxide and H_2O_2 decomposition with $CoFe_2O_4$ as the most active sample. Both reactions exhibited a drastic decrease in activity over the samples containing a higher Fe amount than $CoFe_2O_4$ ($x < 1$). This activity drop was less pronounced in TBHP decomposition, resulting in a slightly different activity order, but the overall trend on TBHP decomposition is very similar to 2-cyclohexene-1-hydroperoxide and H_2O_2 decomposition (Fig. 7).

The rate constants for H_2O_2 decomposition over the $Co_xFe_{3-x}O_4$ series are summarized in Table S3,† again identifying $CoFe_2O_4$ to be the most active catalyst with a rate constant of $k = 0.679\ s^{-1}$. The comparison with $CoFe_2O_4$ spinel samples from literature reports clearly shows a superior catalytic activity of the spray-flame synthesized $CoFe_2O_4$ sample (Table S4†). Cota *et al.*[43] and Goldstein *et al.*,[44] who both had a leading role in the research on peroxide decomposition in the last century, prepared $CoFe_2O_4$ samples enabling surface-area-normalized rate constants of $k_s = 0.071\ s^{-1}\ m^{-2}$ and $k_s = 0.120\ s^{-1}\ m^{-2}$ in alkaline solution, respectively, which are significantly lower compared with our catalyst ($k_s = 0.527\ s^{-1}\ m^{-2}$). Onuchukwu *et al.*[45] also studied H_2O_2 decomposition in alkaline solution over $CoFe_2O_4$ synthesized by co-precipitation and obtained a mass-normalized rate constant of $k_m = 14\ s^{-1}\ g^{-1}$, which is one fifth of the spray-flame synthesized $CoFe_2O_4$ ($k_m = 67.9\ s^{-1}\ g^{-1}$). Mimani *et al.*[46] synthesized $CoFe_2O_4$ by a low-temperature decomposition approach and obtained a reaction rate constant of $k_s = 0.232\ s^{-1}\ m^{-2}$, while $CoFe_2O_4$ materials synthesized by co-precipitation and sol–gel method led to significantly lower reaction rate constants of $k_m = 0.037\ s^{-1}\ g^{-1}$ and $k_s = 0.04\ s^{-1}\ m^{-2}$, respectively.[47,48]

Interestingly, the H_2O_2 decomposition experiments using Co_3O_4 and $CoFe_2O_4$ synthesized by a precursor decomposition approach and direct co-precipitation revealed Co_3O_4 to be more active than $CoFe_2O_4$.[17] This observation can be attributed to the platelet-like structure and the significantly smaller specific surface areas (~30 $m^2\ g^{-1}$) of these catalysts. Furthermore, unlike for the herein presented Co_3O_4, the surfaces of the Co_3O_4 sample in literature synthesized by co-precipitation were (111)-oriented.

Earlier studies on H_2O_2 decomposition over Co- and Fe-based spinels showed that it is not the incorporation of Fe, but rather the change of cation distribution within the spinel structure playing a crucial role in the high catalytic activity of Co–Fe mixed oxide catalysts. This assumption is supported by the low activity over γ-Fe_2O_3. Table S5† shows the theoretical cation valency distribution and spinel type of the prepared samples based on the crystal field stabilization energy of the transition metal ions.[49] With increasing Fe amount incorporated in the spinel structure, a change from normal to inverse spinel and an increase of Co^{2+} ions located at octahedral voids is predicted. This was corroborated by our experimental results from Raman and Mössbauer spectroscopy, showing a clear trend towards a predominantly inverse structure with increasing Fe content.

Anthony and Onuchukwu[50] investigated H_2O_2 decomposition over two series of $Ni_xFe_{3-x}O_4$ and $Cu_xFe_{3-x}O_4$ catalysts. The authors highlighted the importance of the electron exchange by redox couples and were not able to demonstrate any significant influence of Fe present in the spinel samples. Similarly, Onuchukwu and Zuru[45] prepared a $Co_xFe_{3-x}O_4$ spinel series by co-precipitation and investigated its catalytic activity in H_2O_2 decomposition. They found $Co_{1.5}Fe_{1.5}O_4$ to be the best catalyst and explained this observation by the presence of each 0.5 mol Co^{2+} and Co^{3+} per formula unit in the octahedral voids of the spinel, enabling an optimal electron exchange between the redox couple within the octahedral sites.[45] However, H_2O_2 decomposition was carried out in a highly alkaline environment. The present study identifies $CoFe_2O_4$ to be the most active catalyst in acetonitrile, which does not contain the Co^{2+}/Co^{3+} redox couple at the octahedral sites. Mimani and Patil[46] found cobaltites to

significantly better decompose H_2O_2 than ferrites, identifying the importance of Co species for H_2O_2 decomposition.

Goldstein and Tseung[51] also investigated the complete series of $Co_xFe_{3-x}O_4$ in H_2O_2 decomposition with $0 \leq x \leq 3$ under basic conditions and proposed a ranking of redox couples:

$$[Co^{2+}\text{–}Co^{3+}]_O > [Co^{2+}\text{–}Fe^{3+}]_O > (Co^{2+})_T \gg [Fe^{2+}\text{–}Fe^{3+}]_O > (Fe^{2+})_T$$

Based on these results, the superior activity of Co_3O_4 compared with Fe_3O_4 becomes clear, as Co^{2+} ions in tetrahedral voids are much more active than Fe^{2+} ions in octahedral voids. $[Co^{2+}]_O$ exhibited the highest activity in H_2O_2 decomposition. Moreover, a higher activity of $[Co^{2+}]_O$ was found when the adjacent octahedral site ion was Co^{3+} instead of Fe^{3+}. Although 0.5 mol redox couple of Co^{2+}/Co^{3+} is present in the octahedral voids in $Co_{1.5}Fe_{1.5}O_4$, 1 mol $[Co^{2+}]_O$ per formula unit is present in the spinel structure of $CoFe_2O_4$ resulting in the highest concentration of $[Co^{2+}]_O$ in the whole $Co_xFe_{3-x}O_4$ series justifying its outstanding catalytic activity. The samples $x = 1.5$ to $x = 3$ all have the same amount of 1 mol Co^{2+} ions per formula unit present in the spinel structure, but 0.5 mol Co^{2+} is present in octahedral voids for $x = 1.5$. Thus, this sample should have a higher activity, whereas the samples $x = 2$, $x = 2.5$ and $x = 3$ should exhibit similar activities (Table S5†). The comparison of Co_3O_4 ($x = 3$) containing 1 mol $(Co^{2+})_T$ with $Co_{0.5}Fe_{2.5}O_4$ ($x = 0.5$) exhibiting 0.5 mol $[Co^{2+}]_O$ suggests Co_3O_4 to be more active than $Co_{0.5}Fe_{2.5}O_4$, whereas Fe_3O_4 ($x = 0$) is expected to show the lowest activity in terms of H_2O_2 decomposition as it contains no Co^{2+} ions. Based on these considerations, Goldstein and Tseung[44] proposed the following activity ranking for the $Co_xFe_{3-x}O_4$ samples:

$$Co_1 > Co_{1.5} > Co_2 = Co_{2.5} = Co_3 > Co_{0.5} > Co_0$$

This order is fully consistent with the obtained order of the rate constants as a function of the catalyst composition for H_2O_2 and 2-cyclohexene-1-hydroperoxide decomposition (Fig. 7). For TBHP decomposition, the activity order based on the produced O_2 volume is consistent, too, but the area-normalized rate clearly shows deviating results suggesting additional influences on TBHP decomposition besides the catalyst composition. Thus, the high catalytic activity of $CoFe_2O_4$ can be presumably referred to the high concentration of octahedrally coordinated Co^{2+} cations, so that the incorporation of Fe leads to a beneficial change of the cation distribution within the spinel structure, while the Fe cations themselves might play a minor role for the catalytic activity.

The reaction mechanism of H_2O_2 decomposition by ferrous and ferric salts was investigated by Haber and Weiss in 1932 and extended by Barb in 1949.[52,53] They proposed H_2O_2 decomposition to be a radical chain reaction mechanism involving $^{\bullet}OH$ and $HO_2^{\bullet}$ radicals as well as HO^- and HO_2^- anions. Fe^{2+} is proposed to be the active site for H_2O_2 decomposition being oxidized to Fe^{3+} and forming OH^- anions and $^{\bullet}OH$ radicals, which initiate the radical chain reaction. The inferior activity of Fe^{3+} in H_2O_2 decomposition

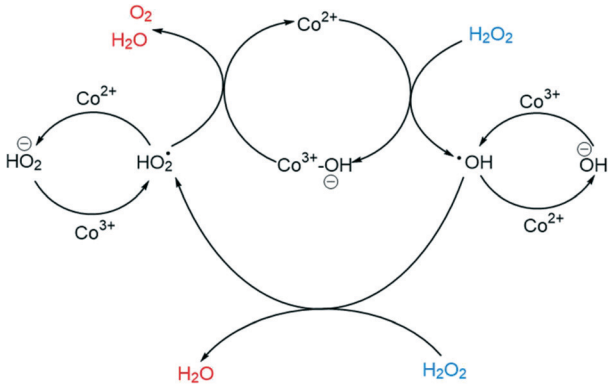

Scheme 2 Proposed reaction mechanism for H_2O_2 decomposition over Co^{2+} based on the Haber–Weiss mechanism.[52,53]

is confirmed by the lowest catalytic performance of γ-Fe_2O_3, which is a Fe^{2+}-free structure. Similar to Fe^{2+} in the Haber–Weiss mechanism presented in Scheme S1,† we propose Co^{2+} to initiate a comparable reaction mechanism of H_2O_2 decomposition with a superior catalytic activity compared with Fe^{2+} and propose an analogous reaction mechanism for H_2O_2 decomposition over Co^{2+} (Scheme 2).

The presence of divalent Co cations at octahedral sites of the spinel structure is thus essential for the decomposition of peroxides. This observation is directly connected to the surface termination of particles, as different facets preferentially expose different cations. Sojka *et al.*[25] investigated the surface structure of spinel nanocrystals by DFT + U calculations and TEM and found the (111) facet to be the most prominent facet with 67.5% of the overall surface area of truncated octahedral $CoFe_2O_4$ nanoparticles. This correlates with our findings, since TEM images of $CoFe_2O_4$ indicate a higher number of truncated octahedral particles with hexagonal and square surface planes (Fig. 1). Moreover, they calculated the surface composition of the (100), (110) and (111) facets by a slab model demonstrating the octahedral cations to be most pronounced on the surface of the (111) facet. For this reason, three-fold coordinated, coordinatively unsaturated Co_{3c}^{2+} species in octahedral sites are highly exposed at $CoFe_2O_4$ nanoparticles acting as most active sites for peroxide decomposition reactions. In contrast, Co_3O_4 particles were reported to predominantly expose the (100) surface, which was also indicated for Co_3O_4 in this study. In cubic Co_3O_4 nanoparticles, five-fold coordinated divalent cations are exposed at the (100) facets, which can be regarded as significantly less active, since more strongly unsaturated cations allow higher catalytic activity. Overall, the coordinatively unsaturated Co_{3c}^{2+} cations at octahedral sites on the (111) terminated surface of $CoFe_2O_4$ can be assumed to be the most active sites for peroxide decomposition.

Conclusions

A series of $Co_xFe_{3-x}O_4$ nanoparticulate catalysts with $x = 3$, 2.5, 2, 1.5, 1, 0.5 and 0 was prepared by spray-flame synthesis and

characterized in-depth by N_2 physisorption, XRD, TEM, XPS, FT-IR, Raman and Mössbauer spectroscopy. The $Co_xFe_{3-x}O_4$ samples were found to have chemical compositions close to the nominal ones, high specific surface areas ranging from 87 to 151 $m^2\ g^{-1}$ and small particle sizes between 8.3 and 12.0 nm. The cation distribution was evaluated by Mössbauer spectroscopy, being consistent with trends also seen in theoretical estimates based on the crystal field stabilization energy. The application of $Co_xFe_{3-x}O_4$ catalysts in cyclohexene oxidation resulted in a volcano plot with the highest catalytic activity at $x = 1$ ($CoFe_2O_4$). Cyclohexene conversion gradually increased with decreasing Co amount from $x = 3$ to $x = 1$. Simultaneously, the selectivity to the key intermediate 2-cyclohexene-1-hydroperoxide decreased, indicating its faster decomposition. Beyond this Co amount ($x < 1$), the catalytic activity strongly decreased again. The product selectivity was poorly affected by the Co and Fe amount incorporated into the $Co_xFe_{3-x}O_4$ catalysts, identifying the catalysts to mainly accelerate the decomposition of the hydroperoxide. Kinetic investigations were performed using the most active catalyst $CoFe_2O_4$ revealing first-order reaction kinetics with an apparent activation energy of 58 kJ mol^{-1}. A reusability test confirmed the excellent stability of the $CoFe_2O_4$ nanoparticles in cyclohexene oxidation. In addition, we were able to decouple 2-cyclohexene-1-hydroperoxide decomposition from the complex reaction network of cyclohexene oxidation by investigating the rates of H_2O_2 and TBHP decomposition. A very good agreement of the decomposition rates of 2-cyclohexene-1-hydroperoxide, H_2O_2 and TBHP was found, identifying $CoFe_2O_4$ as the most active catalyst for all three reactants, suggesting that 2-cyclohexene-1-hydroperoxide is also decomposed following the Haber–Weiss mechanism with octahedral Co_{3c}^{2+} exposed at the (111) facets as the most active sites.

Experimental

Materials

$Co_xFe_{3-x}O_4$ nanoparticles were synthesized using the metal precursors of cobalt(II) nitrate ($Co(NO_3)_2{\cdot}6H_2O$, >99.0%, Honeywell) and iron(III) nitrate ($Fe(NO_3)_3{\cdot}6H_2O$, >99.9%, Sigma-Aldrich). As solvents, ethanol (>99.9%, VWR) and 2-ethylhexanoic acid (>99%, Alfa Aesar) were used.

For cyclohexene oxidation, cyclohexene (99%), 2-cyclohexene-1-one (98%), 2-cyclohexene-1-ol (95%), cyclohexene oxide (98%), 7-oxabicyclo[4.1.0]heptane-2-one (98%), cyclohexane-1,2-diol (98%) and 1,2-dichlorobenzene (99%) were purchased from Sigma-Aldrich. Acetonitrile in analytical reagent grade was bought from Fisher Chemicals. All reagents were employed without further purification.

Catalyst synthesis

The synthesis of spinel nanoparticles was performed in a spray-flame reactor described previously in detail.[54,55] Metal nitrates were used as precursors and dissolved in a mixture of 35 vol% ethanol and 65 vol% 2-ethylhexanoic acid. The precursor solutions contained a total metal-ion concentration of 0.2 M. The solutions were injected *via* syringe pumps to a capillary of an external-mixing atomizing nozzle at a constant flow rate of 2 mL min^{-1}. Fine spray was formed by the interaction of the liquid flow with the dispersion O_2 gas (6 slm, Air Liquide, technical). The spray is ignited by a continuously burning premixed pilot flame of methane (3 slm, Air Liquide, N25, 99.5%) and oxygen (5 slm). The pilot flame itself is surrounded by a sheath-gas flow (140 slm, compressed air) to stabilize the flame and shield it from the reactor walls. Downstream the reaction chamber, a quenching gas flow of compressed air was added to control the sintering of the particles and the off-gas temperature at values lower than 130 °C in order to prevent the damage of the filter membrane which is used to collect the particles during the synthesis process.

Methods

X-ray diffraction patterns were recorded in a PANalytical X'Pert PRO operated with Cu-K_α radiation (0.15406 nm, 40 kV, 40 mA). The diffraction intensity was recorded at 2θ =10–60° with a step size of 0.05°.

N_2 physisorption measurements were performed at 77 K in a Quantachrome Nova2000. The specific surface areas were determined from the adsorption isotherm using the BET method.

$$X = \frac{n_{Cy,0} - n_{Cy}}{n_{Cy,0}}$$

$$S = \frac{n_p - n_{p,0}}{n_{Cy,0} - n_{Cy}}$$

$$r = \frac{1}{m_{cat} \cdot S_{BET}} \cdot \frac{dn_{Cy}}{dt}$$

High-resolution and high-angle annular dark-field scanning transmission electron microscopy (HR-TEM, HAADF-STEM), and energy dispersive X-ray spectroscopy (EDX) measurements were performed at a probe-side aberration-corrected JEM-2200FS (JEOL, Akishima, Japan) with an acceleration voltage of 200 kV.

Fourier-transform infrared spectroscopy was carried out in a Vertex 80 from Bruker using a KBr beam splitter, a DigiTect DLaTGS detector, and a mid-infrared light source from 400 to 4000 cm^{-1} in combination with an ATR sample holder.

Raman spectra were recorded using a Renishaw InVia confocal Raman microscope with a 633 nm laser operating at 1% of the total laser power (15 mW).

X-ray photoelectron spectra were obtained using a ULVAC-PHI device (Versaprobe II) using a XPS twin anode with Mg Kα & Al Kα, a spot size of 100 μm, and an energetic resolution of ~0.5 eV. The calibration of the spectra was done using the C1s adventitious carbon C–C binding energy at 284.8 eV. The obtained data were fitted based on fixed positions, fixed contributions of the specific peaks to the overall signal as well as fixed FWHM. Using this procedure, a

satisfactory overall fit was obtained in which nearly no area was left unfitted.

Mössbauer spectra were recorded in transmission geometry at 4.3 K with and without applying an external magnetic field, using a ^{57}Co(Rh) radiation source, liquid helium (magnet) cryostats, 20–35 mg of each nanoparticle powder and a velocity transducer operating at constant acceleration.

Catalytic oxidation reactions

Oxidation reactions were carried out in a 100 mL autoclave reactor equipped with a Teflon liner (Parr Instruments). 50 mg catalyst were dispersed in 30 mL acetonitrile. 20 mmol cyclohexene and 4.5 mmol 1,2-dichlorobenzene as the internal standard for GC analysis were added. The autoclave was purged with oxygen for three times and pressurized to 10 bar. Subsequently, the reaction mixture was heated to 80 °C. The reaction was initiated by switching on the stirrer to 600 rpm. Samples were taken through an online sampling system after 0.5, 1, 2, 4, and 6 h, and analyzed by GC. The catalyst was separated by centrifugation.

To test the reusability of the catalyst, four reaction runs were carried out under standard conditions. After each run, the catalyst was separated by centrifugation, washed three times with 5 mL acetonitrile, and dried overnight at room temperature.

For the investigation of cyclohexene oxidation in the presence of H_2O, 3 mL H_2O were added to the initial standard solution whereas all other reaction conditions remained unchanged.

Conversion (X), selectivity (S), the area-related reaction rate (r) normalized to the mass (m_{Cat}) and the specific surface area (S_{BET}) of the catalyst were calculated, in which $n_{Cy,\,0}$ and $n_{P,0}$ denote the initial molar amount of cyclohexene and the respective product at t_0, respectively, and n_{Cy} and n_P denote the molar amount of cyclohexene and the respective product at a defined time t. The carbon balance was higher than 97% in all experiments.

Gas chromatography

Gas chromatography analysis was carried out in a 7820 A GC from Agilent Technologies. It was equipped with an Agilent DB-XLB column (30 m × 180 μm × 0.18 μm) and an FID detector. The injection volume was set to 0.5 μL with a split ratio of 75 : 1, a split flow of 30 mL min^{-1}, and an inlet temperature of 260 °C. The column was first kept at 80 °C for 5 min. Subsequently, the oven was heated to 170 °C with a rate of 15 °C min^{-1}. Afterwards, it was heated with a ramp of 30 °C min^{-1} up to 300 °C to avoid deposits of the PPh_3 in the column. The end temperature was kept for 1 min.

TBHP decomposition

TBHP decomposition was carried out in a peroxide decomposition setup (Gasmess-5, Fig. S17†). 50 mg catalyst were dispersed in 30 mL acetonitrile. The solution was heated to 60 °C and stirred at 600 rpm. 500 μL TBHP were added and the gas volume measurement was started immediately. The decomposition reaction was run for 6 h.

H_2O_2 decomposition

H_2O_2 decomposition was carried out in a peroxide decomposition setup (Gassmess-5, Fig. S17†). 10 mg catalyst were dispersed in 30 mL acetonitrile. The solution was kept at 30 °C and stirred at 600 rpm. 80 μL H_2O_2 (30 wt%) were added and the gas volume measurement was started immediately. The decomposition reaction was run for 30 min.

Conflicts of interest

There are no conflicts to declare.

Acknowledgements

This research was funded by the Deutsche Forschungsgemeinschaft (DFG, German Research Foundation, TRR 247 "Heterogeneous Oxidation Catalysis in the Liquid Phase", project number: 388390466). The work is supported by the "Center for Solvation Science ZEMOS" funded by the German Federal Ministry of Education and Research BMBF and by the Ministry of Culture and Research of Nord Rhine-Westphalia. We thank Dr. Hagemann and Dr. Heidelmann (Interdisciplinary Center for Analytics on the Nanoscale (ICAN), University of Duisburg-Essen) for XPS and TEM measurements, respectively.

References

1 I. M. Denekamp, M. Antens, T. K. Slot and G. Rothenberg, Selective Catalytic Oxidation of Cyclohexene with Molecular Oxygen: Radical versus Nonradical Pathways, *ChemCatChem*, 2018, **10**, 1035–1041.
2 Y. Cao, H. Yu, F. Peng and H. Wang, Selective Allylic Oxidation of Cyclohexene Catalyzed by Nitrogen-Doped Carbon Nanotubes, *ACS Catal.*, 2014, **4**, 1617–1625.
3 B. G. Rao, P. Sudarsanam, P. R. Nallappareddy, M. Y. Reddy, T. V. Rao and B. M. Reddy, Selective Allylic Oxidation of Cyclohexene Catalyzed by Nanostructured Ce-Sm-Si Materials, *Catal. Commun.*, 2017, **101**, 57–61.
4 R. Criegee, H. Pilz and H. Flygare, Zur Kenntnis der Olefinperoxyde, *Berichte der deutschen chemischen Gesellschaft (A and B Series)*, 1939, **72**, 1799–1804.
5 S. M. Mahajani, M. M. Sharma and T. Sridhar, Uncatalysed Oxidation of Cyclohexene, *Chem. Eng. Sci.*, 1999, **54**, 3967–3976.
6 V. S. Kirankumar and S. Sumathi, A Review on Photodegradation of Organic Pollutants Using Spinel Oxide, *Mater. Today Chem.*, 2020, **18**, 100355.
7 P. Cousin and R. A. Ross, Preparation of Mixed Oxides: A Review, *Mater. Sci. Eng., A*, 1990, **130**, 119–125.
8 T. Falk, S. Anke, H. Hajiyani, S. Saddeler, S. Schulz, R. Pentcheva, B. Peng and M. Muhler, Influence of the Particle Size on Selective 2-Propanol Gas-Phase Oxidation over Co3O4 Nanospheres, *Catal. Sci. Technol.*, 2021, **11**, 7552–7562.

9 S. Patoux, L. Daniel, C. Bourbon, H. Lignier, C. Pagano, F. Le Cras, S. Jouanneau and S. Martinet, High Voltage Spinel Oxides for Li-Ion Batteries: From the Material Research to the Application, *J. Power Sources*, 2009, **189**, 344–352.

10 C. G. Anchieta, D. Sallet, E. L. Foletto, S. S. Da Silva, O. Chiavone-Filho and C. A. O. do Nascimento, Synthesis of Ternary Zinc Spinel Oxides and their Application in the Photodegradation of Organic Pollutant, *Ceram. Int.*, 2014, **40**, 4173–4178.

11 Y. Sun, H. Liao, J. Wang, B. Chen, S. Sun, S. J. H. Ong, S. Xi, C. Diao, Y. Du and J.-O. Wang, Covalency Competition Dominates the Water Oxidation Structure–Activity Relationship on Spinel Oxides, *Nat. Catal.*, 2020, **3**, 554–563.

12 S. Pal, U. P. Azad, A. K. Singh, D. Kumar and R. Prakash, Studies on Some Spinel Oxides Based Electrocatalysts for Oxygen Evolution and Capacitive Applications, *Electrochim. Acta*, 2019, **320**, 134584.

13 J. Büker, B. Alkan, Q. Fu, W. Xia, J. Schulwitz, D. Waffel, T. Falk, C. Schulz, H. Wiggers and M. Muhler, Selective Cyclohexene Oxidation with O2, H2O2 and Tert-Butyl Hydroperoxide over Spray-Flame Synthesized LaCo1−xFexO3 Nanoparticles, *Catal. Sci. Technol.*, 2020, **10**, 5196–5206.

14 T. Falk, E. Budiyanto, M. Dreyer, C. Pflieger, D. Waffel, J. Büker, C. Weidenthaler, K. F. Ortega, M. Behrens, H. Tüysüz, M. Muhler and B. Peng, Identification of Active Sites in the Catalytic Oxidation of 2-Propanol over Co1+xFe2-xO4 Spinel Oxides at Solid/Liquid and Solid/Gas Interfaces, *ChemCatChem*, 2021, **13**, 2942–2951.

15 D. Waffel, E. Budiyanto, T. Porske, J. Büker, T. Falk, Q. Fu, S. Schmidt, H. Tüysüz, M. Muhler and B. Peng, Investigation of Synergistic Effects between Co and Fe in Co3-xFexO4 Spinel Catalysts for the Liquid-Phase Oxidation of Aromatic Alcohols and Styrene, *Mol. Catal.*, 2020, **498**, 111251.

16 J. Büker, B. Alkan, S. Chabbra, N. Kochetov, T. Falk, A. Schnegg, C. Schulz, H. Wiggers, M. Muhler and B. Peng, Liquid-Phase Cyclohexene Oxidation with O2 over Spray-Flame-Synthesized La1-xSrxCoO3 Perovskite Nanoparticles, *Chem. – Eur. J.*, 2021, **27**, 16912–16923.

17 A. Rabe, J. Büker, S. Salamon, A. Koul, U. Hagemann, J. Landers, K. Friedel Ortega, B. Peng, M. Muhler, H. Wende, W. Schuhmann and M. Behrens, The Roles of Composition and Mesostructure of Cobalt-based Spinel Catalysts in Oxygen Evolution Reactions, *Chem. – Eur. J.*, 2021, **27**, 17038–17048.

18 Y.-I. Jang, H. Wang and Y.-M. Chiang, Room-Temperature Synthesis of Monodisperse Mixed Spinel (CoxMn1−x)3O4 Powder by a Coprecipitation Method, *J. Mater. Chem.*, 1998, **8**, 2761–2764.

19 T. H. Dolla, K. Pruessner, D. G. Billing, C. Sheppard, A. Prinsloo, E. Carleschi, B. Doyle and P. Ndungu, Sol-Gel Synthesis of MnxNi1-xCo2O4 Spinel Phase Materials: Structural, Electronic, and Magnetic Properties, *J. Alloys Compd.*, 2018, **742**, 78–89.

20 Z. Chen, E. Shi, W. Li, Y. Zheng and W. Zhong, Hydrothermal Synthesis and Optical Property of Nano-Sized CoAl2O4 Pigment, *Mater. Lett.*, 2002, **55**, 281–284.

21 M. Seyedahmadian, S. Houshyarazar and A. Amirshaghaghi, Synthesis and Characterization of Nanosized of Spinel LiMn2O4 via Sol-Gel and Freeze Drying Methods, *Bull. Korean Chem. Soc.*, 2013, **34**, 622–628.

22 B. Alkan, D. Medina, J. Landers, M. Heidelmann, U. Hagemann, S. Salamon, C. Andronescu, H. Wende, C. Schulz and W. Schuhmann, Spray-Flame-Prepared LaCo1-xFexO3 Perovskite Nanoparticles as Active OER Catalysts: Influence of Fe Content and Low-Temperature Heating, *ChemElectroChem*, 2020, **7**, 2564–2574.

23 S. Angel, J. Neises, M. Dreyer, K. Friedel Ortega, M. Behrens, Y. Wang, H. Arandiyan, C. Schulz and H. Wiggers, Spray-Flame Synthesis of La(Fe,Co)O3 Nano-Perovskites from Metal Nitrates, *AIChE J.*, 2020, **66**, e16748.

24 B. Varghese, C. H. Teo, Y. Zhu, M. V. Reddy, B. V. R. Chowdari, A. T. S. Wee, V. B. Tan, C. T. Lim and C.-H. Sow, Co3O4 Nanostructures with Different Morphologies and their Field-Emission Properties, *Adv. Funct. Mater.*, 2007, **17**, 1932–1939.

25 F. Zasada, J. Grybos, P. Indyka, W. Piskorz, J. Kaczmarczyk and Z. Sojka, Surface Structure and Morphology of M [CoM′] O4 (M = Mg, Zn, Fe, Co and M′ = Ni, Al, Mn, Co) Spinel Nanocrystals: DFT+ U and TEM Screening Investigations, *J. Phys. Chem. C*, 2014, **118**, 19085–19097.

26 S. Wang, Y. Zhao, H. Xue, J. Xie, C. Feng, H. Li, D. Shi, S. Muhammad and Q. Jiao, Preparation of flower-like CoFe2O4@ graphene composites and their microwave absorbing properties, *Mater. Lett.*, 2018, **223**, 186–189.

27 R. Al-Tuwirqi, A. A. Al-Ghamdi, N. A. Aal, A. Umar and W. E. Mahmoud, Facile Synthesis and Optical Properties of Co3O4 Nanostructures by the Microwave Route, *Superlattices Microstruct.*, 2011, **49**, 416–421.

28 L. J. Cote, A. S. Teja, A. P. Wilkinson and Z. J. Zhang, Continuous Hydrothermal Synthesis of CoFe2O4 Nanoparticles, *Fluid Phase Equilib.*, 2003, **210**, 307–317.

29 G. Gnanaprakash, S. Ayyappan, T. Jayakumar, J. Philip and B. Raj, Magnetic Nanoparticles with Enhanced γ-Fe2O3 to α-Fe2O3 Phase Transition Temperature, *Nanotechnology*, 2006, **17**, 5851.

30 A. Diallo, A. C. Beye, T. B. Doyle, E. Park and M. Maaza, Green Synthesis of Co3O4 Nanoparticles via Aspalathus Linearis: Physical Properties, *Green Chem. Lett. Rev.*, 2015, **8**, 30–36.

31 B. Rivas-Murias and V. Salgueiriño, Thermodynamic CoO-Co3O4 Crossover Using Raman Spectroscopy in Magnetic Octahedron-Shaped Nanocrystals, *J. Raman Spectrosc.*, 2017, **48**, 837–841.

32 Y. Zheng, Y. Yu, H. Zhou, W. Huang and Z. Pu, Combustion of Lean Methane over Co3O4 Catalysts Prepared with Different Cobalt Precursors, *RSC Adv.*, 2020, **10**, 4490–4498.

33 K. Gandha, K. Elkins, N. Poudyal and J. Ping Liu, Synthesis and Characterization of CoFe2O4 Nanoparticles with High Coercivity, *J. Appl. Phys.*, 2015, **117**, 17A736.

34 V. Bartůněk, D. Sedmidubský, Š. Huber, M. Švecová, P. Ulbrich and O. Jankovský, Synthesis and Properties of Nanosized Stoichiometric Cobalt Ferrite Spinel, *Materials*, 2018, **11**, 1241.

35 R. N. Bhowmik and N. Naresh, Structure, ac Conductivity and Complex Impedance Study of Co3O4 and Fe3O4 Mixed Spinel Ferrites, *International Journal of Engineering, Science and Technology*, 2010, **2**, 40–52.
36 R. Sagayaraj, S. Aravazhi and G. Chandrasekaran, Tuning of Ferrites (CoxFe3-xO4) Nanoparticles by Co-Precipitation Technique, *Appl. Sci.*, 2019, **1**, 1–11.
37 A. M. Wahba and M. B. Mohamed, Structural and Magnetic Characterization and Cation Distribution of Nanocrystalline CoxFe3−xO4 Ferrites, *J. Magn. Magn. Mater.*, 2015, **378**, 246–252.
38 M. C. Biesinger, B. P. Payne, A. P. Grosvenor, L. W. Lau, A. R. Gerson and R. S. Smart, Resolving Surface Chemical States in XPS Analysis of First Row Transition Metals, Oxides and Hydroxides: Cr, Mn, Fe, Co and Ni, *Appl. Surf. Sci.*, 2011, **257**, 2717–2730.
39 H. Liu, G. Wei, Z. Xu, P. Liu and Y. Li, Quantitative Analysis of Fe and Co in Co-Substituted Magnetite Using XPS: The Application of Non-Linear Least Squares Fitting (NLLSF), *Appl. Surf. Sci.*, 2016, **389**, 438–446.
40 H. Le Trong, L. Presmanes, E. de Grave, A. Barnabé, C. Bonningue and P. Tailhades, Mössbauer Characterisations and Magnetic Properties of Iron Cobaltites CoxFe3−xO4 ($1 \leq x \leq 2.46$) Before and After Spinodal Decomposition, *J. Magn. Magn. Mater.*, 2013, **334**, 66–73.
41 P. J. Murray and J. W. Linnett, Mössbauer studies in the spinel system CoxFe3− xO4, *J. Phys. Chem. Solids*, 1976, **37**, 619–624.
42 G. M. Bancroft, T. K. Sham, C. Riddle, T. E. Smith and A. Turek, Ferric/Ferrous-Iron Ratios in Bulk Rock Samples by Mössbauer Spectroscopy—The Determination of Standard Rock Samples G-2, GA, W-1 and mica-Fe, *Chem. Geol.*, 1977, **19**, 277–284.
43 H. M. Cota, T. Katan, M. Chin and F. J. Schoenweis, Decomposition of Dilute Hydrogen Peroxide in Alkaline Solutions, *Nature*, 1964, **203**, 1281.
44 J. R. Goldstein and A. C. Tseung, The Kinetics of Hydrogen Peroxide Decomposition Catalyzed by Cobalt-Iron Oxides, *J. Catal.*, 1974, **32**, 452–465.
45 A. I. Onuchukwu and A. B. Zuru, The Cobalt-Ferrite, CoxFe3−xO4, Activity in the Catalytic Chemical Decomposition of Hydrogen Peroxide, *Mater. Chem. Phys.*, 1986, **15**, 131–138.
46 T. Mimani, P. Ravindranathan and K. C. Patil, *Catalytic Decomposition of Hydrogen Peroxide on Fine Particle Ferrites and Cobaltites*, Springer, 1987, vol. 4.
47 P. Lahiri and S. K. Sengupta, Spinel Ferrites as Catalysts: A Study on Catalytic Effect of Coprecipitated Ferrites on Hydrogen Peroxide Decomposition, *Can. J. Chem.*, 1991, **69**, 33–36.
48 T. Tatarchuk, A. Shyichuk, I. Trawczyńska, I. Yaremiy, A. T. Pędziwiatr, P. Kurzydło, B. F. Bogacz and R. Gargula, Spinel cobalt (II) ferrite-chromites as catalysts for H2O2 decomposition: Synthesis, morphology, cation distribution and antistructure model of active centers formation, *Ceram. Int.*, 2020, **46**, 27517–27530.
49 U. Müller, *Anorganische Strukturchemie*, Vieweg+Teubner Verlag/ GWV Fachverlage GmbH Wiesbaden, Wiesbaden, 6th edn, 2008.
50 A. I. Onuchukwu, Kinetics of the Decomposition of Hydrogen Peroxide Catalysed by Copper and Nickel Ferrites, *J. Chem. Soc., Faraday Trans. 1*, 1984, **80**, 1447–1456.
51 A. C. Tseung and J. R. Goldstein, The Preparation and Characterization of Ultrafine Cobalt-Iron Oxides, *J. Mater. Sci.*, 1972, **7**, 1383–1390.
52 F. Haber and J. Weiss, The Catalytic Decomposition of Hydrogen Peroxide by Iron Salts, *Proc. R. Soc. London, Ser. A*, 1934, **147**, 332–351.
53 W. G. Barb, J. H. Baxendale, P. George and K. R. Hargrave, Reactions of Ferrous and Ferric Ions with Hydrogen Peroxide. Part I.—The Ferrous Ion Reaction, *Trans. Faraday Soc.*, 1951, **47**, 462–500.
54 S. Angel, F. Schneider, S. Apazeller, W. Kaziur-Cegla, T. C. Schmidt, C. Schulz and H. Wiggers, Spray-Flame Synthesis of LaMO3 (M= Mn, Fe, Co) Perovskite Nanomaterials: Effect of Spray Droplet Size and Esterification on Particle Size Distribution, *Proc. Combust. Inst.*, 2021, **38**, 1279–1287.
55 S. Hardt, I. Wlokas, C. Schulz and H. Wiggers, Impact of Ambient Pressure on Titania Nanoparticle Formation During Spray-Flame Synthesis, *J. Nanosci. Nanotechnol.*, 2015, **15**, 9449–9456.